


## Research Article

# Investigation on Pore-Fracture of Coal and Its Influence Mechanism on Tensile Failure Behavior of Coals with Bursting Proneness

Yutao Li,<sup>1</sup> Qingwei Guo,<sup>1</sup> Xunchen Liu ,<sup>2</sup> Yaodong Jiang,<sup>3</sup> Bo Zhang,<sup>4</sup> and Hao Wang<sup>5</sup>

<sup>1</sup>School of Civil Engineering and Architecture, Nanyang Normal University, Nanyang 473061, China

<sup>2</sup>Department of Railway Engineering, Shijiazhuang Institute of Railway Technology, Shijiazhuang 050041, China

<sup>3</sup>School of Mechanics and Civil Engineering, China University of Mining and Technology (Beijing), Beijing 100083, China

<sup>4</sup>Emergency Science Research Institute, China Coal Research Institute, Beijing 100013, China

<sup>5</sup>School of Energy and Mining Engineering, China University of Mining and Technology, Beijing 100083, China

Correspondence should be addressed to Xunchen Liu; liuxunch@163.com

Received 22 August 2021; Accepted 22 September 2021; Published 6 October 2021

Academic Editor: Peng Hou

Copyright © 2021 Yutao Li et al. This is an open access article distributed under the Creative Commons Attribution License, which permits unrestricted use, distribution, and reproduction in any medium, provided the original work is properly cited.

Both computed tomography (CT) and notched semicircular bend (NSCB) tests are performed for coals with high and medium bursting proneness to extract the scientific expression of pore-fracture and its influence mechanism on the tensile failure behavior. The acoustic emission (AE) parameters in the sample during loading and failure are monitored, and the influence mechanism of pore-fracture on tensile failure behavior of coal is analyzed. The result illustrates that the spatial distribution feature of the pore-fracture in coals with high and medium bursting proneness is extremely different. The deformation and failure mode of the coals are affected by many factors, loading mode, notch depth and width, mechanical properties of matrix and mineral, spatial distribution feature of pore-fracture, etc. The influence of primary pore-fracture in the coal on the extension and penetration of the secondary fracture could be divided into two types: bifurcation and promotion, which would cause different local damage in the sample and affect the final failure mode. The feature of acoustic emission parameters indicates that the deformation and failure process of a sample under loading could be divided into four stages: compaction stage, elastic deformation stage, displacement plastic growth stage, and post peak failure stage, which is the result of comprehensive action of many factors. The evolution process of secondary fracture is accompanied by the dissipation of elastic strain energy and the intensification of internal damage of coal, which reflects the failure process of coal.

## 1. Introduction

Coal possesses important position in China's energy strategic system in recent years, which is supportive role to economic development. It could be predicted that coal will still be the dominant energy in China within a long term in the future [1, 2]. However, it is inevitable for deep coal mining with the depletion of shallow coal resources [3–6]. There is a significant difference between them; comprehensive analysis results demonstrate that all the higher geostress, higher geotemperature, and higher osmotic pressure in the deep coal seams change the mechanical properties and stress state of coal existing in shallow coal seams, resulting in frequent deep

dynamic disasters [7–9]. In the mining process, the coal is normally in a complex stress state of tension and compression coexisting; however, its tensile strength is far lower than the compressive strength. It is important to make a profound and comprehensive research on its tensile performance for the coal seam stability and dynamic disaster prevention.

Coal is a complex porous medium formed by plant remains under the combined action of geology and biology. It is well accepted that coal is composed of organic components (matrix), inorganic components (mineral), and pore-fracture [10–12]. The existence of pore-fracture aggravates the complexity of coal and forms the storage space and migration channel of gas and other fluids, also affecting the

mechanical properties and failure behavior of coal under external load. Scholars at home and abroad have studied the pore-fracture in coal and achieved fruitful results. Various methods are employed to study the pore-fracture in coal, such as mercury intrusion porosimetry (MIP), gas adsorption ( $N_2/CO_2/CH_4$ ), computerized tomography (CT), nuclear magnetic resonance (NMR), scanning electron microscopy (SEM), and transmission electron microscopy (TEM), which could be divided into three types, i.e., direct observations of the surface morphology, fluid intrusion methods, and X-ray and spectroscopic methods [13, 14]. Guo et al. proposed coal seam permeability measurement based on the new permeability evolution model, which is conducive to intensive study of permeability during its plastic deformation [15]. Zhao et al. studied the feature of pores by using synchrotron radiation nano-CT and nuclear magnetic resonance technology (NMR) and realized the visualization of the pore throat structure [16, 17]. Zhu et al. analyzed the relationship between pore properties and dynamic disaster of coal and pointed out that there were differences in pore between coals with bursting proneness and gas outburst [18]. Wu et al. calculated the dynamic elastic parameters of coal through experimental mensuration and theoretical analysis and concluded that the dynamic elastic parameters were related to fracture in the coal [19]. Peng et al. analyzed the fracture morphology of coals both before and after triaxial compression failure based on CT technology and constructed the fractal model for fracture distribution [20]. Nie et al. used gas adsorption and SEM tests to characterize the pore in different rank coals and considered that the pore was related to its coalification process and metamorphic degree [21]. Wang et al. analyzed the fracture of high rank coal by CT and mercury intrusion porosimetry (MIP) and approved that the fracture shape was related to the permeability of coal [22]. Bastola and Cai proposed the relation between fracture propagation and mechanical properties of marble based on the lattice-spring-based synthetic rock mass model (LS-SRM) and found that different fracture parameters have different effects on mechanical properties [23]. Du et al. analyzed the fracture of Changzhi Coal Mine and its influence on permeability by the scanning electron microscope energy spectrum and adsorption test and established the pore-fracture network model [24]. Li et al. built the multifractal model of dual porous media and analyzed the relationship between fracture structure and permeability [25]. Manjunath and Jha studied the nanoscale fracture mechanics properties of coal by experiment and theoretical calculation [26]. Wei et al. analyzed the full-scale pore feature of deep coal seams in Huainan Coal Mine and its influence on adsorption capacity by comprehensive application of MIP, nitrogen/carbon dioxide adsorption, and electron microscope scanning experiments [27]. Pan et al. compared the pros and cons of the common experimental techniques used to measure the pore in coal, SEM, AFM, etc., and analyzed the feature of pore-fracture through fractal theory [28]. Mou et al. suggested that metamorphism, tectonic deformation, and matrix are the main internal factors affecting the pore distribution in coal [13]. Cai et al. and Wang et al. studied the evolution of faults in rockburst dynamic disasters by

means of field investigation and theoretical analysis and considered that the weak surfaces such as faults changed the static and dynamic stresses in the region, dominating the fault reactivation, which would be an induced factor of rockburst [29–31]. Jiang et al. researched the fault parameters' influence on the burst through field microseismic monitoring and numerical analyses [32]. Teng et al. systematically researched the influence of pore-fracture on coal seam gas migration from the aspects of experiment, numerical simulation, and model establishment and proposed new measures to improve the drainage efficiency, which obtained good engineering results [33–36]. The test measures of tensile mechanical properties of coal in the laboratory include the direct tensile test and indirect tensile test [37, 38].

In summary, the present researches about pore-fracture in coal mainly concentrate on the feature of the pore-fracture and relationship among pore-fracture, permeation, and adsorption-desorption. Achievements have been achieved in the research approaches and methods, the feature of pore-fracture with different scales in the coal, and influence of external factors (temperature, stress, water, etc.) on pore-fracture. However, few reports on the relationship between pore-fracture and tensile properties of coal have been published. The tensile properties of coal are affected by geological conditions, gas occurrence in coal, and pore-fracture, and it is hard to be accurately determined through existing technology. There are many methods that could be used to test the tensile properties of coal, such as the chevron bend (CB) and shortrod (SR) specimens, the cracked chevron notched Brazilian disc (CCNBD) specimen, and the notched semicircular bend (NSCB) specimen, which are divided into the direct test and indirect test. It is accepted that the latter is simpler operating and more accurate than the former. The NSCB test belongs to the latter and is widely used [39, 40]. The coals with high and medium bursting proneness are chosen for study; the spatial distribution feature of the pore-fracture and its influence mechanism on the tensile failure behavior of coal are investigated through CT and NSCB tests; the acoustic emission signal during deformation and failure under external load is monitored to validate the internal damage evolution process of coal.

## 2. Materials and Methods

*2.1. Sample Preparation.* Samples with high and medium bursting proneness are collected from Hongqinghe Coal Mine (HQH) and Nalinhe Coal Mine (NLH), respectively. The position of samples is shown in Figure 1. For the former, it is located in Yijinholo Banner, Ordos City, Inner Mongolia Autonomous Region, China. It is a monoclonal structure with a dip of  $1^\circ$ – $3^\circ$ ; folds and faults are not developed and fall within gas free coal mine. Only No. 3 coal seam had up to 10 times destructive burst during the mining period from March to November 2018, which caused roadway damage and equipment damage. The samples are derived from No. 9 coal seam with an average buried depth of about 760 m. For the latter, it is close to Hongqinghe Coal Mine, which is located in Wushen Banner, Ordos City, Inner Mongolia Autonomous Region, China. The roof of No. 3 coal seam



FIGURE 1: Location of the coals with high and medium bursting proneness.

mainly belongs to the unstable roof, locally belonging to the medium stable type, and the floor belongs to the relatively soft (IIIa) type. The samples are taken from No. 3 coal seam, which has experienced many microseismic events, and the average buried depth is 600 m or thereabout. The samples are carefully and rapidly sent to a laboratory and then drilled into a semicylinder with dimensions of 50 mm in diameter and 25 mm in height. Both ends are trimmed to ensure that the unevenness is less than 0.01 mm, and the side is polished to make sure that the nonparallelism is not greater than 0.01 mm. The notches with 1 mm in width and 6/8 mm in length are machined at the center of the circle, and the top is sharpened by a diamond wire saw. The numbering rule of samples is the abbreviation of the coal mine; the width of the notch is the serial number of the sample. For example, N8-2 represents the sample from Nalinhe Coal Mine with 8 mm in width, and the order is 2. Industrial analysis and axial wave velocity tests are performed before CT and NSCB, and the results are illustrated in Table 1 [10].

**2.2. Experimental and Monitoring Method.** The CT test is carried out at the State Key Laboratory of Coal Resources and Safe Mining of China University of Mining and Technology, Beijing, and the equipment is ACTIS300320-225, which could perform precise and accurate detection of the 3D structure inside the sample. In order to improve the reliability of the results, the CT test complies with Chinese National Standard GB/T26593-2011. During the test, the scanning interval in the height direction is  $50\ \mu\text{m}$ , and 501 pictures are scanned for every sample, which are recorded as 1-501 from bottom to top. The picture size is  $1050 \times 525$  pixels, and the resolution of each pixel is about  $50\ \mu\text{m}$ , which could characterize the pore-fracture in the sample. A detailed description of the test process is shown in Li et al. [10].

Before the NSCB test, two measures are adopted to monitor the damage information of samples. Firstly, two groups of strain gauges are pasted on the surface of every sample to record the strain during failure. Notably, the strain gauges

TABLE 1: Results of industrial analysis and axial wave velocity test of coal specimens.

Samples	Fixed carbon (%)	Ash content (%)	Volatile matter (%)	Moisture (%)	Axial wave velocity (m/s)
Hongqinghe	56.59	7.17	28.20	8.05	850-950
Nalinhe	37.26	18.11	38.57	6.05	850-920

are located on the straight line connected with the loading point at the upper end and the notch and 2 mm away from them, numbered 1 and 2, respectively. It is important to state that the strain gauge is BX120-5AA, and the four channel DH3821 static strain test and analysis system are selected to collect strain information, as shown in Figure 2. The micro-II express acoustic emission detection system produced by American Physical Acoustics Corporation is employed to record and analyze the acoustic emission signals in the failure process of samples. In the test, two acoustic emission sensors numbered 1 and 2 are selected, and the connecting line of the sensor center is perpendicular to the cross-section of the sample. After being coated with Vaseline, the sensors are fixed on the surface of the sample to improve the contact quality between sensors and the sample. The equipment of NSCB is the Electronic Universal Testing Machine MTSC45.104 produced in the United States, as shown in Figure 3. The loading was displacement controlled, and the loading speed was 0.1 mm/min. During the test, a specially assigned person would be responsible for the loading equipment, acoustic emission detection equipment, and strain test system, respectively, so the environment is quiet, and all these tests are synchronized.

### 3. Results and Analysis

**3.1. Analysis of Pore-Fracture in the Coal.** CT is nondestructive detection technology and extensively used in the research of mesodamage mechanical properties and internal component analysis of porous material, such as coal and shale. It could realize continuous and multiple scanning records of different sections of the sample and also realize 3D reconstruction and display the three-dimensional structure of the sample [41–45]. The principle of CT is that X-rays passing through substances with different densities would be attenuated to varying degrees and show different colors (gray value) on the images. The higher density of substances implies more attenuation and lighter color on the image. Therefore, three components of matrix, mineral, and pore-fracture in the coal could be identified through ternary gray threshold segmentation, i.e., the black part of the image represents pore-fracture, the dark gray part indicates matrix, and the light-colored part means mineral [46–49]. Original images attained through CT are usually 16-bit grayscale images, which need pretreatment for 3D reconstruction of the sample. The pretreatment includes background recognition (distinguish and adjust the gray value in the background region of the image through MATLAB program), artifact and noise elimination (regulate the deviant gray value

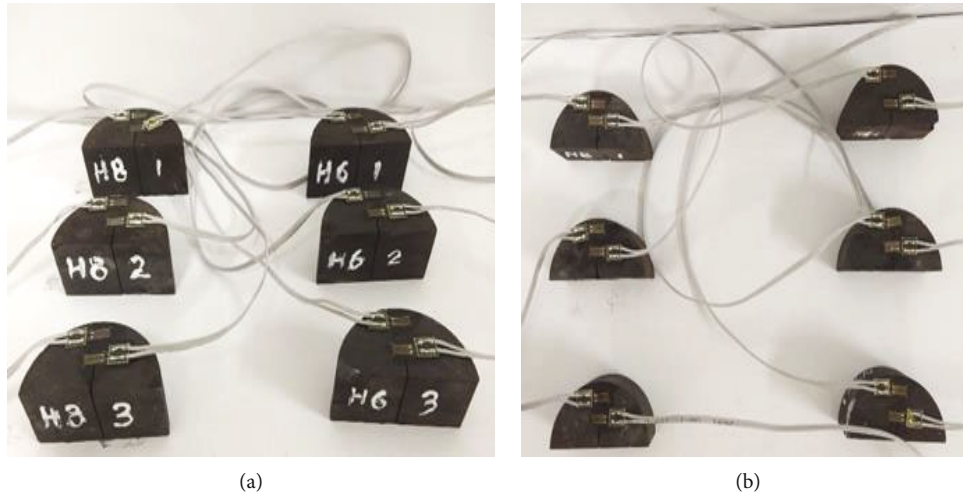


FIGURE 2: Samples for NSCB: (a) samples from HQH; (b) samples from NLH.

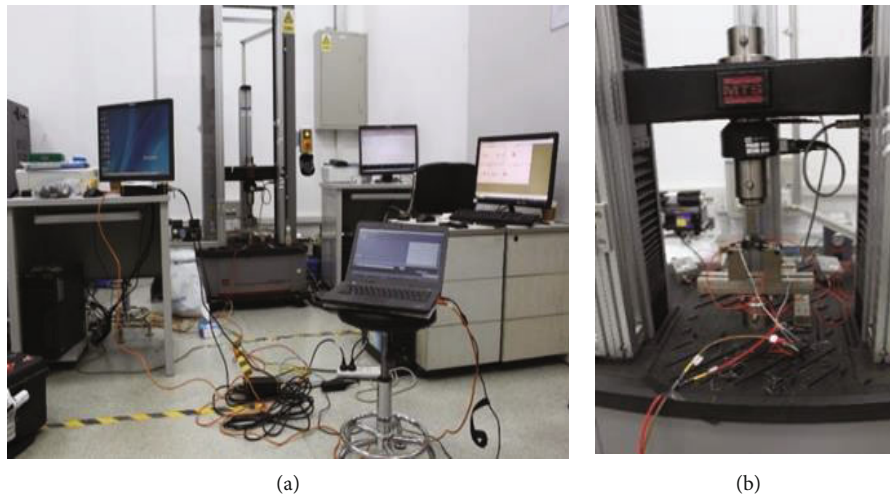


FIGURE 3: Diagram of equipment and sample for NSCB test: (a) equipment diagram of NSCB test; (b) equipment diagram of loading and sample.

caused by the improper operating voltage through MATLAB), and fuzzy edge renovation (utilize the prewitt operator in MATLAB), which is described in detail in Li et al. [10]. MATLAB is an extraordinary extensively practical image processing software, which provides a synthetical set of algorithms and workflow apps for image processing, analysis, visualization, and algorithm development and could be used in microscale image processing of porous materials [50, 51]. The author-compiled MATLAB program is introduced to segment the CT image based on the value of gray. The processed image only includes three kinds of gray values, corresponding to minerals, matrix, and pore-fracture from small to large. Taking the No. 207 image of the sample from HQH as an example, images before and after ternary processing are shown in Figures 4(a) and 4(b), which demonstrate the distribution of the three components in the coal.

Plenty of software could complete the 3D reconstruction of CT images, such as MATLAB, AVIZO, and MIMICS, etc. [42, 43, 52]. MIMICS possesses the advantages of mature

technology, simple operation, high image recognition, and compatibility with numerical simulation software, ANSYS, FLAC3D, etc., and is used to image import, image segmentation, image visualization, and image measurement. MIMICS is selected for the 3D reconstruction in the study, and the results of samples with a notch of 6 mm in width are illustrated in Figure 5. It indicates that the spatial distribution of the components in the coal is random, and the volume proportion of matrix, mineral, and pore-fracture is shown in Table 2. A large number of pore-fracture coexist in coal, with different widths, lengths, and morphology, and the spatial distribution feature of pore-fracture among the samples is apparently different. Specifically, pore-fracture in samples from HQH is relatively scattered, and the connectivity is poor. While pore-fracture in samples from NLH is characterized by regional differences, the connectivity has increased. Pore-fracture is the mechanical property weak point of a sample during deformation and failure under load; different scale pore-fractures have different evolution laws during the deformation and failure process of samples with different levels of



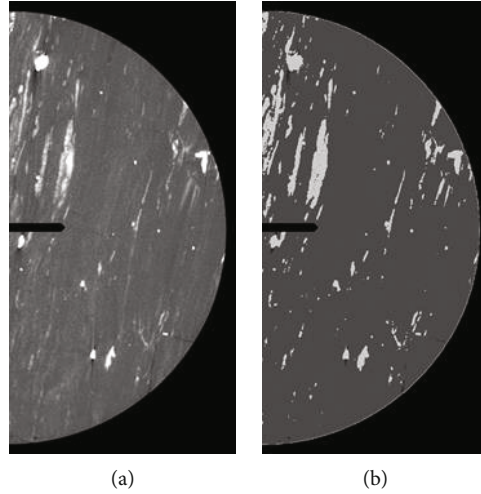


FIGURE 4: No. 207 CT images before and after ternary processing: (a) No. 207 CT image of sample from HQH before ternary processing; (b) No. 207 CT image of sample from HQH after ternary processing.

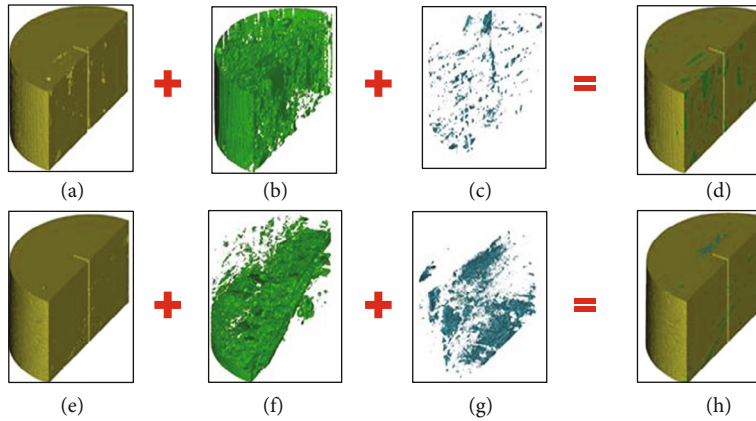


FIGURE 5: 3D reconstruction of samples from HQH and NLH with notch of 6 mm in width: (a) matrix of sample from HQH; (b) mineral of sample from HQH; (c) pore-fracture of sample from HQH; (d) 3D reconstruction of sample from HQH; (e) matrix of sample from NLH; (f) mineral of sample from NLH; (g) pore-fracture of sample from NLH; (h) 3D reconstruction of sample from NLH.

TABLE 2: Volume proportion of components in the sample.

Samples	Pore-fracture	Mineral	Matrix	Total
HQH	8.95%	19.51%	71.54%	100%
NLH	10.49%	17.13%	72.38%	100%

bursting proneness, which affects the failure mode of the sample.

**3.2. Load-Displacement Analysis of Loading Point.** Despite the reinforcement measures being taken, some problems still occurred during the test, such as rapid destruction of samples and falling off of the strain gauges, which cause the lack of some strain test data. The load-displacement curve of samples at the loading point during the test is shown in Figure 6, and the data of N8-2 was lost. It demonstrates that the failure process of the sample includes the compaction stage, elastic deformation stage, displacement plastic growth stage, and post peak failure stage, and the displacement plas-

tic growth stage is not obvious. The maximum load of samples in HQH decreases when the width of the sample changes from 6 mm to 8 mm. The post peak load decreased in steps to varying degrees, indicating that the main bearing structure of the sample changed, and the sound could be heard clearly during the test. After the bearing structure failed, the load decreased sharply, resulting in the destruction of coal samples. Notably, data of H8-1 are much larger than that of samples in the same group, which are considered to disperse. The maximum load of samples from NLH does not change obviously under different widths of notches, the compaction stage is relatively gentle, and the displacement at the loading point is relatively large. For N6-1 and N6-2, post peak load of the former drops sharply and the sample damages, while that of the latter drops in multilevel steps. The results of samples with 8 mm in width are different from the others. Among them, the N8-2 damages too fast and the results are not obtained. The compaction stage of N8-1 is short; the load in the post peak stage decreases in multilevel steps, accompanied by elastic energy dissipation. The N8-3

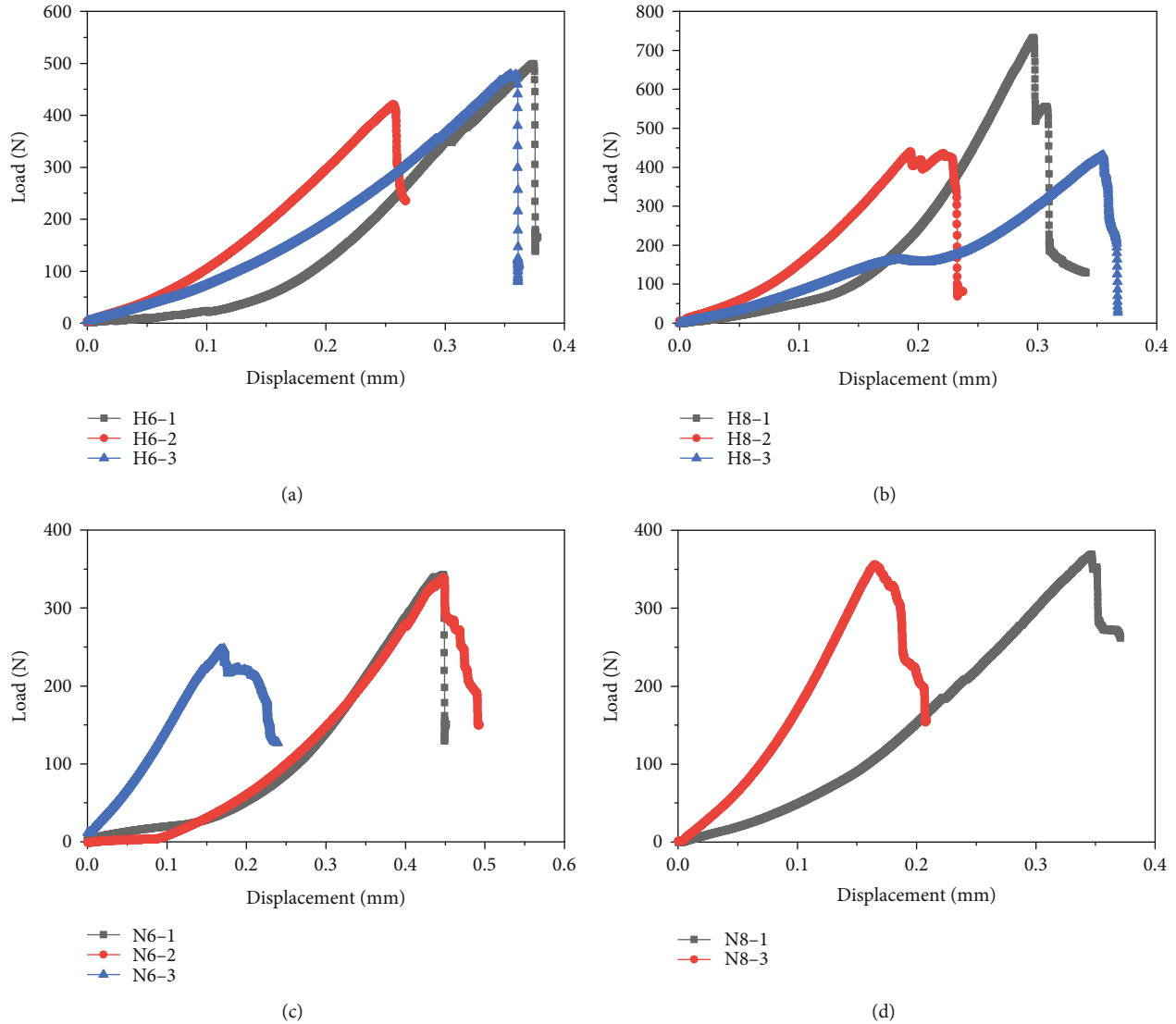


FIGURE 6: Diagram of the load-displacement of samples.

damages rapidly after the elastic deformation stage, and the residual strength is greater than N8-1. It could conclude that the failure behavior of the sample is related to its level of bursting proneness, the width of the notch, and other factors, under the same loading mode. The average maximum load of samples from HQH (high bursting proneness) is greater than that of NLH (medium bursting proneness), and the failure process is more sudden and thorough; even some strain gauges destroy completely. The larger width of notch would attenuate the maximum load of samples from HQH severely, and little for that of NLH.

**3.3. Strain-Time Analysis of Detection Points.** The strain-time curve of detection points under external load is shown in Figure 7, and data of some detection points are not effectively obtained. Two strain gauges of H6-1 and No. 2 of H6-2 were lost during the test, and the destruction time of N8-2 is too short; these data are missing. If the width of the notch is 6 mm, strains of H6-2 and H6-3 are much smaller than that of the others, which drop rapidly after the peak value.

Vicinity of No. 1 strain gauge in H6-2 mainly takes compressive stress at an early stage of loading, and tensile stress gradually. Vicinity of No. 1 strain gauge in H6-3 mainly takes compressive stress, and that of No. 2 strain gauge takes tensile stress; brittleness of coal is evident. If the width of the notch is 8 mm, vicinity of No. 2 strain gauges of samples from HQH takes tensile stress, and that of No. 1 strain gauges takes compressive stress; the strain is large. The failure feature of samples from NLH is different from that of HQH, mainly reflected in the step decline of the strain after the peak, which presents differences in the internal structure of them.

**3.4. Acoustic Emission Feature Analysis.** Acoustic emission is a nondestructive monitoring method widely used to detect the deformation and fracture feature of coal and rock materials. It could effectively represent the strain energy liberation of materials and the evolution process of pore-fracture. The 3D position and energy information of micro-fracture events could be obtained through acoustic emission

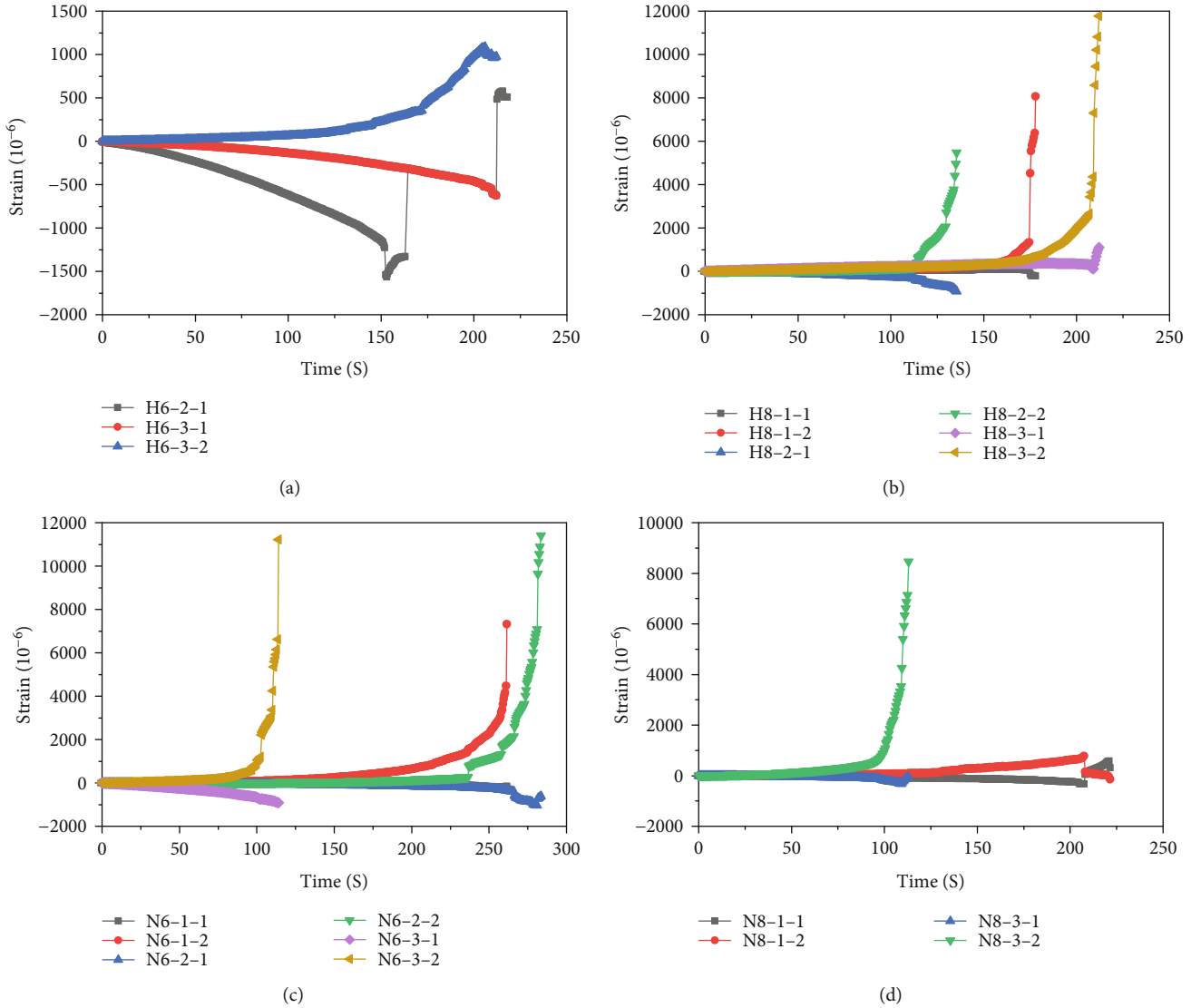


FIGURE 7: Diagram of the strain-time of samples.

TABLE 3: Scheme of AE physical parameters of samples.

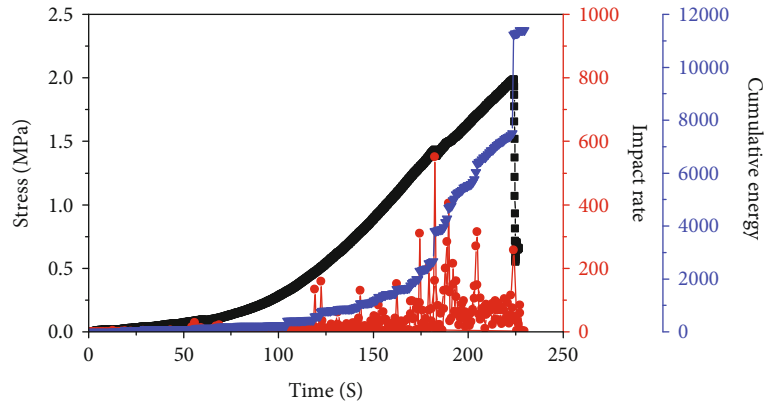
Samples	Cumulative energy ( $10^5$ )	Maximum impact rate	Tensile strength (MPa)
H6-1	1.14	551	1.99
H8-3	0.86	534	1.67
N6-2	1.07	147	1.35
N8-1	1.05	728	1.47

time-frequency parameter analysis, 3D positioning, seismic source mechanism inversion, and related technologies and reproduce the real-time evolution process of secondary fracture in materials [41, 53].

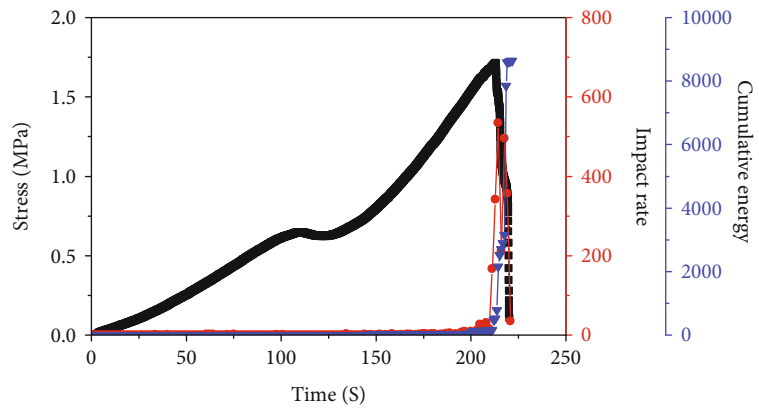
**3.4.1. Acoustic Emission Physical Parameters of Samples.** The threshold value of the acoustic emission signal in the test is set to 40 dB, and the sampling rate is set to 1 MHz. The lead breaking test is performed before loading to ensure that the

acoustic emission signal could be obtained effectively. The timing synchronization of the acoustic emission system and testing machine system is conducted to ensure that the collected data are synchronized in time. Personnel and equipment should keep a safe distance because of the phenomenon that small coal blocks may eject during damage, and the environment in the test should be dark and quiet to improve data accuracy. The results indicate that the acoustic emission characteristics of 12 coal samples were very discrete, and it is extremely difficult and meaningless to analyze the result of all the samples one by one. H6-1, H8-3, N6-2, and N8-1 are selected for analysis, and the relevant results are shown in Table 3. The tensile strength of samples is calculated by Equation (1), according to the suggestions of Zhao et al. [38]:

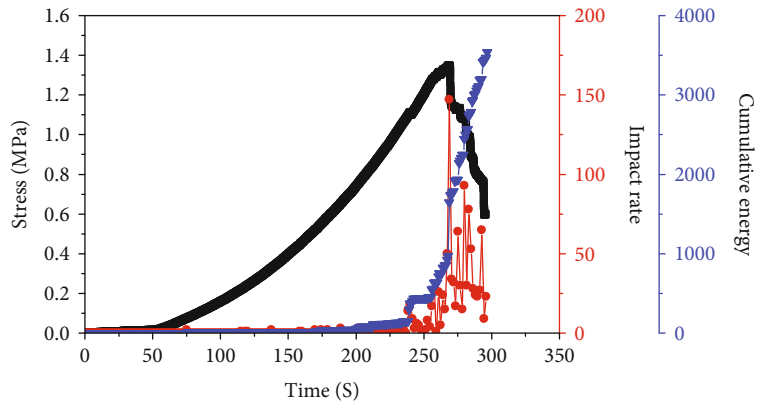
$$\sigma = \frac{4.976P_{\max}}{D \times t}, \quad (1)$$



(a)



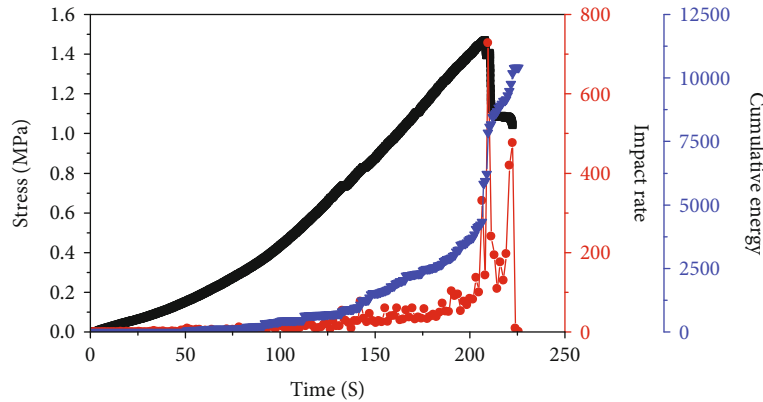
(b)



(c)

FIGURE 8: Continued.





(d)

FIGURE 8: Diagram of the acoustic emission parameters-time of samples.

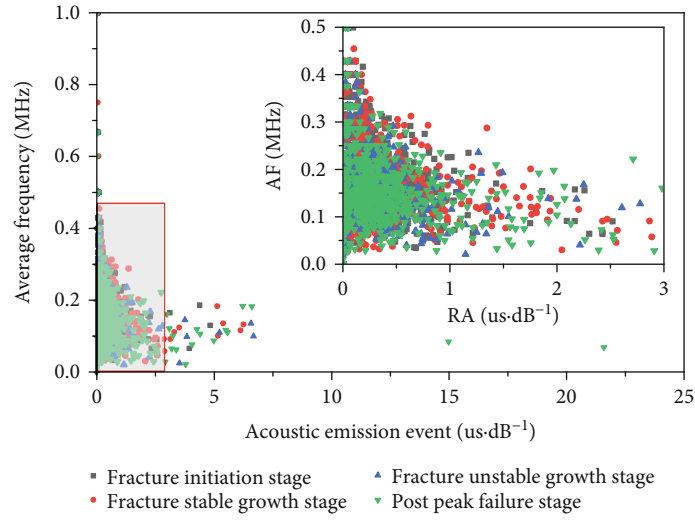
where  $\sigma$  infers to the tensile strength of sample (MPa),  $P_{\max}$  represents the maximum of load (N),  $D$  is diameter of the sample and is a constant equal to 100 (mm), and  $t$  stands for thickness of the sample and equals to 25 (mm).

**3.4.2. Analysis of Acoustic Emission Feature of Samples.** The relationship of H6-1, H8-3, N6-2, and N8-1 in the NSCB test between evolution feature of stress, cumulative energy, impact rate, and time is demonstrated in Figures 8(a)–8(d), respectively. It indicates that mechanical responses of the four samples in four stages are distinctly different, i.e., compaction stage, elastic deformation stage, displacement plastic growth stage, and post peak failure stage. However, the evolutionary process of the parameters is basically consistent with the failure process of the internal structure of the sample. The compaction stage of H6-1 sustains long, and the cumulative energy and impact rate increase slowly, and the growth rate of the other three stages increases. The impact rate increases rapidly in the displacement plastic growth stage, but the value is not large, which indicates that damage in this stage is mainly microfracture extension. The impact rate decreases rapidly, and cumulative energy increases sharply in the post peak failure stage, which means damage is severe and residual stress is small. The acoustic emission feature of H8-3 and N6-2 in the first three stages are not obvious, but the impact rate fluctuates greatly with time in the last stage, which manifests that the failure of samples is not completed instantaneously. The failure duration of the latter is significantly longer than that of the former, which is due to the high bursting proneness of the former. The acoustic emission feature of N8-1 is weak in the compaction stage and enhanced in the other stages, especially in the displacement plastic growth stage. The impact rate fluctuates in the post peak failure stage and coincides with the step failure behavior of samples, which indicates that bearing structure changes during the failure process.

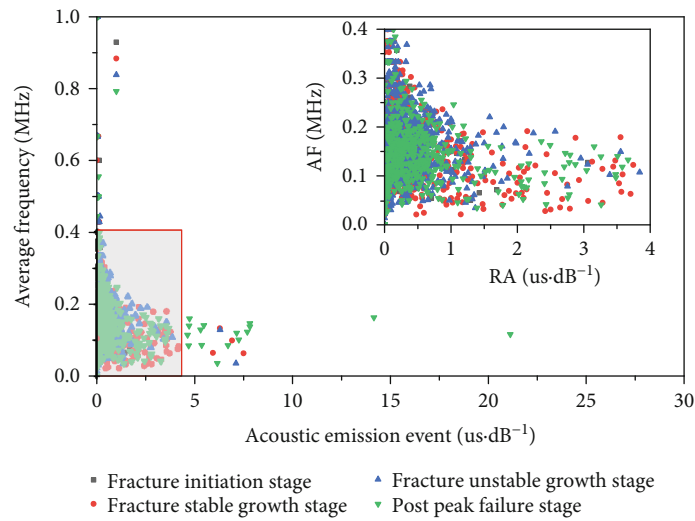
The relationship of H6-1, H8-3, N6-2, and N8-1 in the NSCB test between acoustic emission event RA value (rise time/amplitude) and average frequency AF value (count/duration) is shown in Figures 9(a)–9(d), respectively. Under the suggestion of Liu et al. [54], the acoustic emission wave-

form during the evolution of different types of fractures is various. Generally, the RA value of tensile fracture is low and the AF value is high, the RA value of shear fracture is high and the AF value is low, and the RA value and AF value of tensile shear mixed failure are relatively low. The RA and AF values of coals in this research are scattered and have weak regularity, which indicates that the evolution process of the secondary fracture in the coal is very complex and highly discrete, and all the tensile failure, shear failure, and tensile shear mixed failure coexist during the failure. The acoustic emission signal points in the post peak failure stage are significantly more than that in other stages, which indicates that the duration of the failure process is short, and the failure intensity is large. For H6-1 and H8-3, the width of notch increases; the acoustic emission events with high AF value and low RA value are significantly reduced in the first three stages, which signifies that the tensile fracture in the coal is reduced. Acoustic emission events increase and distribute widely in the displacement plastic growth stage, which indicates that many types of fractures coexist. The acoustic emission events with low AF value and high RA value increase in the post peak failure stage, which shows the increase of shear fracture. For N6-2 and N8-1, the width of notch increases; acoustic emission events are few in the compaction stage; that with high AF value and low RA value increases in the displacement plastic growth stage; likewise, that with low AF value and high RA value increases too. These indicate that both tensile fracture and shear fracture increase, and tensile shear mixed failure occurs in samples.

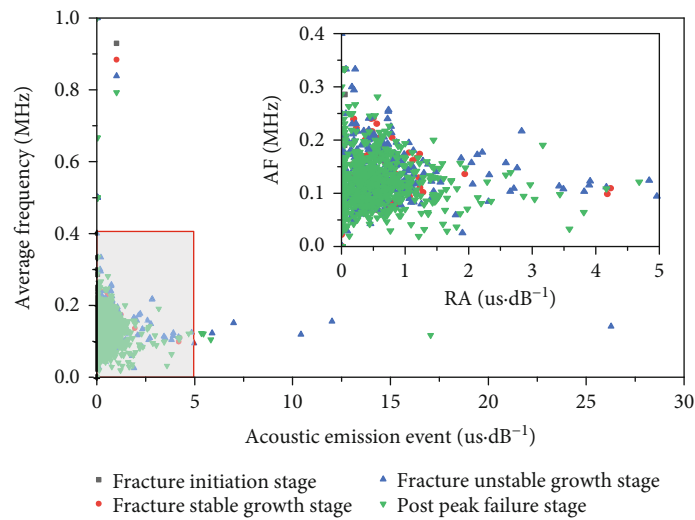
**3.5. Failure Mode Analysis of Samples.** The failure mode of samples in the NSCB test is significantly different, which is shown in Figure 10. The main performance of the main fracture position is not fixed (mostly in and nearby the vertical line at notch or in and nearby the vertical line at the two support points), angles with horizontal line are various (mostly approximately  $90^\circ$  nearby the secondary fracture and change in extension), the extension track is random (affected by the mechanical properties of the coal and the distribution of solid particles, the mineral particles with large hardness would shift or bifurcate the fracture), and the



(a)



(b)



(c)

FIGURE 9: Continued.

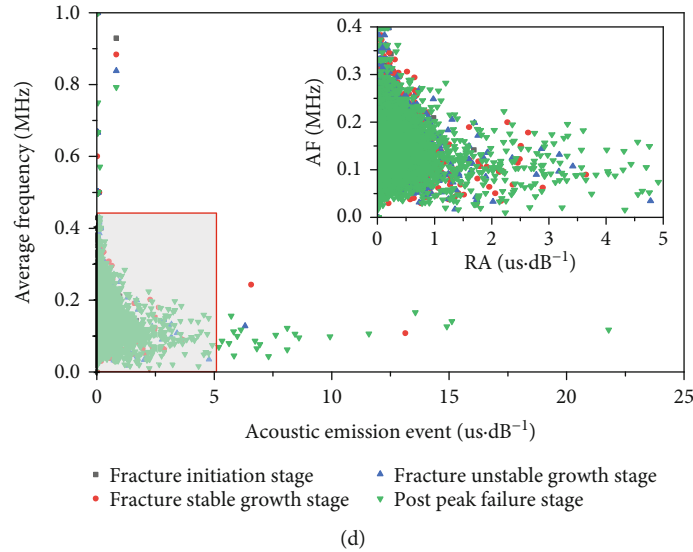


FIGURE 9: Diagram of the acoustic emission AF-RA of samples.



FIGURE 10: Failure mode of samples in the NSCB test.

TABLE 4: Finite element information of components in the sample.

Samples	Number of pore-fracture	Number of minal	Number of matrix	Number of total element	Calculated porosity
HQH	128	279	1023	1430	8.95%
NLH	150	245	1035	1430	10.49%

penetration degree is not fixed (some samples have complete tension fracture and nearly complete penetration of the two strain gauges, and some samples have multiple cracks with similar width and length, but the penetration degree is small). Through strain and acoustic emission information detection, it is considered that the failure behavior of samples in the NSCB test is affected by an external load, mechanical properties of matrix and minal, pore-fracture, and other factors, among which pore-fracture has effect on the deformation in the first three stages. However, the failure mode of the sample is mainly determined by its internal bearing structure evolution and overall mechanical properties.

#### 4. Numerical Simulation Analysis of the Samples

**4.1. Construction of Finite Element Model.** The finite element method is employed to simulate the failure behavior of samples under NSCB conditions. Firstly, the geometric model of sample is established in ANSYS and meshed to calculate the total number of elements, and the element number of every component is calculated based on the volume ratio of that obtained from CT; the finite element information of components in the sample is shown in Table 4. Secondly, the corresponding random order of every component is generated by the author-compiled MATLAB program as its finite element unit number. Notably, if the same finite element unit number of any component appears, it would regenerate until all the numbers are not repeated. Then, elements are selected according to the number and defined as the minal group (minal component), the matrix group (matrix component), and pore-fracture group (pore-fracture component) to construct the finite element model. Taking samples with notch of 8 mm in width as an example, the finite element models of samples from HQH and NLH are shown in Figure 11. The red unit represents the pore-fracture component, the blue unit refers to the minal component, and the green unit stands for the matrix component.

**4.2. Estimation of Material Properties.** Assume that mechanical properties of the minal and matrix component unit in the sample basically conform to Weibull distribution, and the mechanical parameters of them could obtain Vickers hardness test. The microhardness test equipment is the EM-1500L micro Vickers hardness tester. The sample is a cube with 20 mm side length, which is processed and shaped once. The surface of the sample is smooth and flat, and the dust formed in the processing is removed. Three measuring points in the representative matrix and minal area for every sample are discussed and determined by 3-5 operators, and the constant load of 10gf lasts for 15s. Take the average

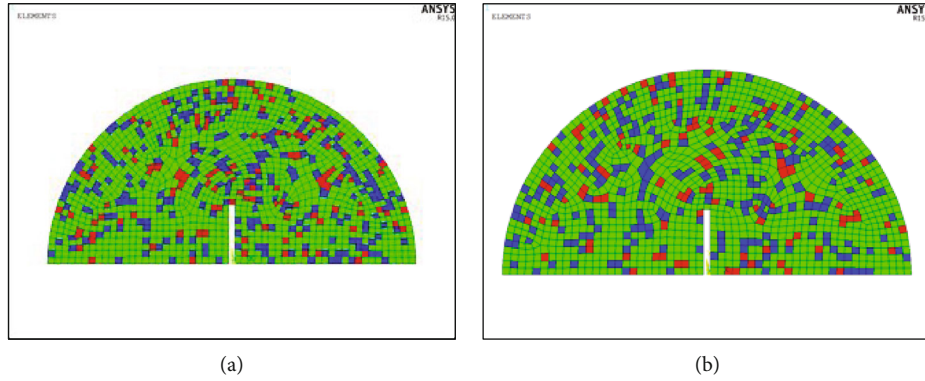


FIGURE 11: Finite element model of sample: (a) finite element model of sample from HQH; (b) finite element model of sample from NLH.

TABLE 5: Hardness of minerals and matrix of samples.

Samples	Component	Hardness value (kg/mm <sup>2</sup> )			Average value (kg/mm <sup>2</sup> )
HQH	Minal	166.93	181.80	155.66	168.13
	Matrix	18.30	18.65	19.87	18.94
NLH	Minal	131.18	130.08	133.87	131.71
	Matrix	30.62	28.88	29.95	29.82

values as the test result, which are shown in Table 5. Mechanical parameters such as elastic modulus and Poisson's ratio of matrix and minal are determined based on the relationship between hardness value and material mechanical parameters, and the results are shown in Table 6. Although the method employed to determine the mechanical parameters has a disadvantage, it could meet the accuracy requirements of mechanical calculation and numerical simulation [55–58]. In the simulation, fixed constraints are applied to the nodes 20 mm away from the center of the circle at the bottom of the model, and a concentrated load is applied to the upper part of the model. Take the node 2 mm above the notch as the detection point (the element should be matrix group), and its stress and strain features are analyzed.

**4.3. Analysis of Numerical Simulation.** The numerical simulation results of the samples from HQH and NLH are shown in Table 7. It considers that the external load, the width of notch, and the mechanical properties of matrix and minal all affect the stress and strain distribution of the detection point. It is well-accepted that the internal stress and strain of symmetrical structure are symmetrically distributed under the action of symmetrical load, but the internal stress and strain distribution of numerical simulation results are much complex and asymmetric. The main reasons are as follows: (1) Spatial distribution of three components in the sample is asymmetric and random. (2) Bearing capacity of the three components in the sample is very different. The coal is heterogeneous and anisotropic, and the local mechanical properties of different positions in the sample are also various. (3) The evolution process of stress and strain in the model under load is complex and has great local differences. The results of numerical simulation indicate that the

internal stress of samples from HQH is much greater than that of NLH, and the strain reverses under the same width of the notch. Additionally, both stress and strain of samples from the same coal mine decrease with the width growth of the notch. Failure position in the sample (stress and strain are great) is basically near the loading point or support point, which would extend to the inner sample. The phenomenon of the tensile zone and stress concentration at different degrees appears nearby the top of the notch. Secondary fracture initiates and extends upward under the continuous action of external load.

## 5. Discussion

**5.1. Influence of External Load on Failure Behavior.** In the NSCB test, the samples all experience the compaction stage, elastic deformation stage, displacement plastic growth stage, and post peak failure stage, accompanied by damage evolution and energy release in the sample. All of these are the mechanical responses under the external load. It concludes that the external load affects the mechanical responses greatly, which is an inducing factor of its failure behavior and could be artificially adjusted.

**5.2. Influence of Mechanical Properties of Matrix and Minal on the Failure Behavior.** Matrix and minal together constitute the bearing structure of the sample, which is the foundation of maintaining the integrity of the sample and postponing the extension and penetration of secondary fracture. Under specific external load, the stress field and strain field would change with the mechanical properties of the matrix and minal. The results of the experiment and numerical simulation indicate that extension and penetration of secondary fracture are almost all along the abrupt region of mechanical properties, such as junction of matrix and minal, junction of matrix and primary pore-fracture, and junction of minal and primary pore-fracture. The tensile strength of matrix and minal is lower than compressive strength. Samples in the NSCB test usually experience tensile failure, shear failure, or tensile shear mixed failure.

**5.3. Influence of Pore-Fracture on the Failure Behavior.** Plenty of randomly distributed pore-fracture forms in the

TABLE 6: Mechanical parameters of minerals and matrix of samples.

Samples	Component	Elastic modulus (GPa)	Poisson's ratio	Cohesion (Pa)	Friction angle (°)	Dilatancy angle (°)
HQH	Minal	38.88	0.20	—	—	—
	Matrix	4.16	0.33	1.56e6	32	0
NLH	Minal	29.59	0.18	—	—	—
	Matrix	3.88	0.26	2.25e6	35	0

TABLE 7: Results of numerical simulation.

Number of the samples	External load (N)	Stress at the detection point (MPa)	Strain at the detection point
H6	480	1.90	0.031%
H8	450	1.76	0.025%
N6	320	1.37	0.042%
N8	300	1.29	0.033%

coalification process, which destroys the integrity of coal and composes the potential point of damage and destruction of the sample. Most of the secondary fracture in the NSCB test initiates near the primary pore-fracture and extends along the weak parts of mechanics. Interestingly, the extension would delay if matrix or minal solid particles are encountered in the extension process. Otherwise, the secondary fracture would accelerate the extension (the directions of secondary fracture and primary fracture are close or consistent) or bifurcation (the directions of secondary fracture and primary fracture are at a certain angle, and this phenomenon is not obvious because of its small tensile strength), and secondary fracture and primary fracture would converge into new loading weak points and continue to extend, resulting in the destruction of the sample eventually. The evolution process of pore-fracture is accompanied by the dissipation of elastic strain energy and the intensification of damage in the coal, which reflects the failure process of coal. The results are consistent with the previous research conclusions [49]. Specifically, the influence of pore-fractures with different geometric parameters on the failure behavior of samples is various, which could hardly be quantitatively analyzed because of the limited research methods and complex influencing factors. Nowadays, the relationship between fracture with certain geometric parameters and failure feature of samples under specific mechanical conditions is studied mainly by numerical simulation and experiment [59, 60].

**5.4. Influence of Notch on the Failure Behavior.** The existence of notch reduces the effective bearing area of the sample and changes the stress feature under the external load, and the NSCB is widely employed in the research of tensile properties. The depth, width of the notch, and the ratio of support point spacing to diameter would all affect failure behavior and failure mode of the sample. The experimental and numerical simulation results both show that the stress and strain values of the detection point change with different parameters of the notch.

## 6. Conclusion

The pore-fracture feature of coals with high and medium bursting proneness is obtained through CT, and the acoustic emission signal during the deformation and failure process of coals in the NSCB test are monitored. The correlation between pore-fracture feature and failure behavior of coals with high and medium bursting proneness is investigated through experiment and numerical simulation. The main conclusions are as follows:

- (1) The failure behaviors of coals with high and medium bursting proneness in the NSCB test are apparently different, and the main differences manifested in the main fracture position is not fixed, the angle between the chief fracture and the horizontal line is various, the extension trajectory of the main fracture is random, and the penetration degree of the main fracture is not fixed. All the differences are comprehensive action of external load, mechanical properties of matrix and minal, and spatial distribution of solid particles and pores and fractures, and the available condition could be merely analyzed from the statistics
- (2) The feature of acoustic emission signals for the coals with high and medium bursting proneness in the NSCB test is different and basically consistent with the damage and failure process of the internal coal. The failure mode of coals is the coexistence of tensile failure, shear failure, and tensile shear failure. The duration of the post peak failure stage for coal with high bursting proneness is very short, the dissipation of elastic strain energy is relatively intense, and mutation occurs in acoustic emission signals. Meanwhile, the duration of the post peak failure stage for coal with medium bursting proneness increases, post peak stress descends multistep, and the acoustic emission signal fluctuates
- (3) The result of the NSCB test demonstrates that external load is the external cause (leading factor) causing the failure of coal, which could be adjusted. Additionally, the mechanical properties of matrix and minal in the coal are the internal cause (important factor), which could not be adjusted. The spatial distribution of matrix, minal, and pore-fracture determines the internal damage evolution and the initiation-extension process of the secondary fracture, and the parameters of notch also affect the test results. The main fracture of coal with high bursting



proneness penetrates rapidly and normally occurs strength failure. The main fracture of coal with medium bursting proneness usually occurs strength failure or instability failure, and the bearing system changes under the comprehensive action of both external cause and internal cause. The influence of primary pore-fractures with different geometric parameters on the extension of main fractures and the failure feature of samples still need to be further studied

## Data Availability

The data used to support the results of the study are available from the corresponding author upon request.

## Conflicts of Interest

The authors declare that they have no conflicts of interest.

## Acknowledgments

The research was supported by the National Natural Science Foundation of China (Nos. 52074301 and 41872205), Beijing Natural Science Foundation (8202041), and State Key Research Development Program of China (2016YFC0801401). These sources of supports are gratefully acknowledged.

## References

- [1] S. Han, H. Chen, R. Long, and X. Cui, "Peak coal in China: a literature review," *Resources, Conservation and Recycling*, vol. 129, pp. 293–306, 2018.
- [2] F. Liu, W. Cao, J. Zhang, G. Cao, and L. Guo, "Current technological innovation and development direction of the 14th five-year plan period in China coal industry," *Journal of China Coal Society*, vol. 46, pp. 1–15, 2021.
- [3] L. Yuan, "Research progress of mining response and disaster prevention and control in deep coal mines," *Meitan Xuebao/Journal China Coal Soc.*, vol. 46, pp. 716–725, 2021.
- [4] W. Wang, H. Li, Y. Liu, M. Liu, H. Wang, and W. Li, "Addressing the gas emission problem of the world's largest coal producer and consumer: lessons from the Sihe Coalfield, China," *Energy Reports*, vol. 6, pp. 3264–3277, 2020.
- [5] H. Xie, F. Gao, Y. Ju et al., "Quantitative definition and investigation of deep mining," *Meitan Xuebao/Journal China Coal Soc.*, vol. 40, pp. 1–10, 2015.
- [6] L. Yuan, "Strategic thinking of simultaneous exploitation of coal and gas in deep mining," *Meitan Xuebao/Journal China Coal Soc.*, vol. 41, pp. 1–6, 2016.
- [7] X. Lian, H. Hu, T. Li, and D. Hu, "Main geological and mining factors affecting ground cracks induced by underground coal mining in Shanxi Province, China," *International Journal of Coal Science & Technology*, vol. 7, no. 2, pp. 362–370, 2020.
- [8] M. He, "Research progress of deep shaft construction mechanics," *Meitan Xuebao/Journal China Coal Soc.*, vol. 46, pp. 726–746, 2021.
- [9] H. Xie, M. Gao, C. Fu et al., "Mechanical behavior of brittle-ductile transition in rocks at different depths," *Meitan Xuebao/Journal China Coal Soc.*, vol. 46, pp. 701–715, 2021.
- [10] Y. Li, Y. Zhao, Y. Jiang, B. Zhang, H. Song, and B. Liu, "Characteristics of pore and fracture of coal with bursting proneness based on DIC and fractal theory," *Energies*, vol. 13, no. 20, p. 5404, 2020.
- [11] M. Bednarz and D. McLroy, "Organism-sediment interactions in shale-hydrocarbon reservoir facies – three-dimensional reconstruction of complex ichnofabric geometries and pore-networks," *International Journal of Coal Geology*, vol. 150–151, pp. 238–251, 2015.
- [12] S. Opluštil, Z. Šimůnek, J. Pšenička, J. Bek, and M. Libertín, "A 25 million year macrofloral record (Carboniferous-Permian) in the Czech part of the Intra-Sudetic Basin; biostratigraphy, plant diversity and vegetation patterns," *Review of Palaeobotany and Palynology*, vol. 244, pp. 241–273, 2017.
- [13] P. Mou, J. Pan, Q. Niu, Z. Wang, Y. Li, and D. Song, "Coal pores: methods, types, and characteristics," *Energy and Fuels*, vol. 35, no. 9, pp. 7467–7484, 2021.
- [14] G. Wang, D. Han, X. Qin, Z. Liu, and J. Liu, "A comprehensive method for studying pore structure and seepage characteristics of coal mass based on 3D CT reconstruction and NMR," *Fuel*, vol. 281, p. 118735, 2020.
- [15] H. Guo, H. Tang, Y. Wu, K. Wang, and C. Xu, "Gas seepage in underground coal seams: application of the equivalent scale of coal matrix-fracture structures in coal permeability measurements," *Fuel*, vol. 288, p. 119641, 2021.
- [16] Y. Zhao, Y. Sun, S. Liu, Z. Chen, and L. Yuan, "Pore structure characterization of coal by synchrotron radiation nano-CT," *Fuel*, vol. 215, pp. 102–110, 2018.
- [17] Y. Zhao, Y. Sun, S. Liu, K. Wang, and Y. Jiang, "Pore structure characterization of coal by NMR cryoporometry," *Fuel*, vol. 190, pp. 359–369, 2017.
- [18] J. Zhu, B. Zhang, Y. Zhang, J. Tang, and Y. Jiang, "Coal pore characteristics in different coal mine dynamic disasters," *Arabian Journal of Geosciences*, vol. 11, pp. 1–10, 2018.
- [19] H. Wu, S. Dong, D. Li, Y. Huang, and X. Qi, "Experimental study on dynamic elastic parameters of coal samples," *International Journal of Mining Science and Technology*, vol. 25, no. 3, pp. 447–452, 2015.
- [20] R. Peng, Y. Ju, J. G. Wang, H. Xie, F. Gao, and L. Mao, "Energy dissipation and release during coal failure under conventional triaxial compression," *Rock Mechanics and Rock Engineering*, vol. 48, no. 2, pp. 509–526, 2015.
- [21] B. Nie, X. Liu, L. Yang, J. Meng, and X. Li, "Pore structure characterization of different rank coals using gas adsorption and scanning electron microscopy," *Fuel*, vol. 158, pp. 908–917, 2015.
- [22] X. Wang, J. Pan, K. Wang, T. Ge, J. Wei, and W. Wu, "Characterizing the shape, size, and distribution heterogeneity of pore-fractures in high rank coal based on X-ray CT image analysis and mercury intrusion porosimetry," *Fuel*, vol. 282, p. 118754, 2020.
- [23] S. Bastola and M. Cai, "Investigation of mechanical properties and crack propagation in pre-cracked marbles using lattice-spring-based synthetic rock mass (LS-SRM) modeling approach," *Computers and Geotechnics*, vol. 110, pp. 28–43, 2019.
- [24] Z. Du, X. Zhang, Q. Huang, S. Zhang, and C. Wang, "Investigation of coal pore and fracture distributions and their contributions to coal reservoir permeability in the Changzhi block, middle-southern Qinshui Basin, North China," *Arabian Journal of Geosciences*, vol. 12, no. 16, 2019.

- [25] B. Li, R. Liu, and Y. Jiang, "A multiple fractal model for estimating permeability of dual-porosity media," *Journal of Hydrology*, vol. 540, pp. 659–669, 2016.
- [26] G. L. Manjunath and B. Jha, "Nanoscale fracture mechanics of Gondwana coal," *International Journal of Coal Geology*, vol. 204, pp. 102–112, 2019.
- [27] Q. Wei, X. Li, J. Zhang et al., "Full-size pore structure characterization of deep-buried coals and its impact on methane adsorption capacity: a case study of the Shihezi Formation coals from the Panji Deep Area in Huainan Coalfield, Southern North China," *Journal of Petroleum Science and Engineering*, vol. 173, pp. 975–989, 2019.
- [28] J. Pan, K. Wang, Q. Hou, Q. Niu, H. Wang, and Z. Ji, "Micropores and fractures of coals analysed by field emission scanning electron microscopy and fractal theory," *Fuel*, vol. 164, pp. 277–285, 2016.
- [29] Z. Ma, Y. Jiang, Y. Li, Y. Yang, and H. Li, "Experimental research on influence of loading rate and confining pressure on energy evolution of coal," *Yantu Gongcheng Xuebao/Chinese J. Geotech. Eng.*, vol. 38, pp. 2114–2121, 2016.
- [30] W. Cai, L. Dou, G. Si, and Y. Hu, "Fault-induced coal burst mechanism under mining-induced static and dynamic stresses," *Engineering*, vol. 7, no. 5, pp. 687–700, 2021.
- [31] H. Wang, R. Shi, D. Deng, Y. Jiang, G. Wang, and W. Gong, "Characteristic of stress evolution on fault surface and coal bursts mechanism during the extraction of longwall face in Yima mining area, China," *Journal of Structural Geology*, vol. 136, p. 104071, 2020.
- [32] L. Jiang, P. Kong, P. Zhang et al., "Dynamic analysis of the rock burst potential of a longwall panel intersecting with a fault," *Rock Mechanics and Rock Engineering*, vol. 53, no. 4, pp. 1737–1754, 2020.
- [33] T. Teng, W. Wang, and P. Zhan, "Evaluation criterion and index for the efficiency of thermal stimulation to dual coal permeability," *Journal of Natural Gas Science and Engineering*, vol. 68, p. 102899, 2019.
- [34] T. Teng, J. G. Wang, F. Gao, and Y. Ju, "Complex thermal coal-gas interactions in heat injection enhanced CBM recovery," *Journal of Natural Gas Science and Engineering*, vol. 34, pp. 1174–1190, 2016.
- [35] T. Teng, Y. Zhao, F. Gao, J. G. Wang, and W. Wang, "A fully coupled thermo-hydro-mechanical model for heat and gas transfer in thermal stimulation enhanced coal seam gas recovery," *International Journal of Heat and Mass Transfer*, vol. 125, pp. 866–875, 2018.
- [36] T. Teng, Y. Xue, and C. Zhang, "Modeling and simulation on heat-injection enhanced coal seam gas recovery with experimentally validated non-Darcy gas flow," *Journal of Petroleum Science and Engineering*, vol. 177, pp. 734–744, 2019.
- [37] J. Wu and L. Yan, "Comparison study on two kinds of indirect measurement methods of tensile strength of coal in lab," *Chinese J. Rock Mech. Eng.*, vol. 23, pp. 1643–1647, 2004.
- [38] Y. Zhao, S. Gong, Y. Jiang, and C. Han, "Characteristics of tensile strength and fracture properties of coal based on semi-circular bending tests. Yanshilixue Yu Gongcheng Xuebao/Chinese J," *Rock Mech. Eng.*, vol. 35, pp. 1255–1264, 2016.
- [39] Y. Zhao, S. Gong, X. Hao, Y. Peng, and Y. Jiang, "Effects of loading rate and bedding on the dynamic fracture toughness of coal: laboratory experiments," *Engineering Fracture Mechanics*, vol. 178, pp. 375–391, 2017.
- [40] F. Dai, M. D. Wei, N. W. Xu, T. Zhao, and Y. Xu, "Numerical investigation of the progressive fracture mechanisms of four ISRM- suggested specimens for determining the mode I fracture toughness of rocks," *Computers and Geotechnics*, vol. 69, pp. 424–441, 2015.
- [41] C. Jiang, X. Liu, W. Wang, W. Wei, and M. Duan, "Three-dimensional visualization of the evolution of pores and fractures in reservoir rocks under triaxial stress," *Powder Technology*, vol. 378, pp. 585–592, 2021.
- [42] G. Wang, J. Shen, S. Liu, C. Jiang, and X. Qin, "Three-dimensional modeling and analysis of macro-pore structure of coal using combined X-ray CT imaging and fractal theory," *International Journal of Rock Mechanics and Mining Sciences*, vol. 123, p. 104082, 2019.
- [43] X. Shi, J. Pan, Q. Hou et al., "Micrometer-scale fractures in coal related to coal rank based on micro-CT scanning and fractal theory," *Fuel*, vol. 212, pp. 162–172, 2018.
- [44] P. Hou, X. Liang, Y. Zhang, J. He, F. Gao, and J. Liu, "3D multi-scale reconstruction of fractured shale and influence of fracture morphology on shale gas flow," *Natural Resources Research*, vol. 30, no. 3, pp. 2463–2481, 2021.
- [45] P. Hou, X. Liang, F. Gao, J. Dong, J. He, and Y. Xue, "Quantitative visualization and characteristics of gas flow in 3D pore-fracture system of tight rock based on lattice Boltzmann simulation," *Journal of Natural Gas Science and Engineering*, vol. 89, p. 103867, 2021.
- [46] X. Liang, P. Hou, Y. Xue, X. Yang, F. Gao, and J. Liu, "A fractal perspective on fracture initiation and propagation of reservoir rocks under water and nitrogen fracturing," *Fractals*, vol. 29, 2021.
- [47] S. Mazumder, K. H. A. A. Wolf, K. Elewaut, and R. Ephraim, "Application of X-ray computed tomography for analyzing cleat spacing and cleat aperture in coal samples," *International Journal of Coal Geology*, vol. 68, no. 3–4, pp. 205–222, 2006.
- [48] Z. Li, D. Liu, Y. Cai, P. G. Ranjith, and Y. Yao, "Multi-scale quantitative characterization of 3-D pore-fracture networks in bituminous and anthracite coals using FIB-SEM tomography and X-ray M-CT," *Fuel*, vol. 209, pp. 43–53, 2017.
- [49] Y. Jing, R. T. Armstrong, H. L. Ramandi, and P. Mostaghimi, "Coal cleat reconstruction using micro-computed tomography imaging," *Fuel*, vol. 181, pp. 286–299, 2016.
- [50] X. Yang, T. Ren, and L. Tan, "Size distribution measurement of coal fragments using digital imaging processing," *Measurement*, vol. 160, p. 107867, 2020.
- [51] T. Li, B. Yao, Y. Liu, and D. Wang, "Grouting fractured coal permeability evolution based on industrial CT scanning," *Geofluids*, vol. 2021, 12 pages, 2021.
- [52] J. P. Mathews, Q. P. Campbell, H. Xu, and P. Halleck, "A review of the application of X-ray computed tomography to the study of coal," *Fuel*, vol. 209, pp. 10–24, 2017.
- [53] R. Shen, H. Li, E. Wang et al., "Mechanical behavior and AE and EMR characteristics of natural and saturated coal samples in the indirect tensile process," *Journal of Geophysics and Engineering*, vol. 16, no. 4, pp. 753–763, 2019.
- [54] B. Liu, Y. Zhao, H. Zhang, and Y. Yuan, "Acoustic emission characteristics of coal under uniaxial compression and Brazilian splitting," *Caikuang yu Anquan Gongcheng Xuebao/journal min. Saf Eng.*, vol. 37, pp. 613–621, 2020.
- [55] Y. Zhao, H. Song, S. Liu, C. Zhang, L. Dou, and A. Cao, "Mechanical anisotropy of coal with considerations of realistic microstructures and external loading directions," *International*

- Journal of Rock Mechanics and Mining Sciences*, vol. 116, pp. 111–121, 2019.
- [56] Y. Zhao, S. Liu, G. Zhao, E. Derek, Y. Jiang, and J. Han, “Journal of geophysical research : solid earth,” *AGU J. Geophys. Res. Solid Earth*, vol. 120, pp. 1195–1209, 2014.
- [57] Z. Ma, R. Pathegama Gamage, and C. Zhang, “Application of nanoindentation technology in rocks: a review,” *Geomechanics and Geophysics for Geo-Energy and Geo-Resources*, vol. 6, no. 4, 2020.
- [58] J. Zhong, Z. Wang, L. Wang, J. Zhao, W. Ren, and H. Zhou, “Characteristics of damage evolution of deep coal based on CT three-dimensional reconstruction,” *Journal of China Coal Society*, vol. 44, pp. 1482–1494, 2019.
- [59] Y. Liu, G. Han, W. Wang, Z. Huo, and T. Meng, “Evolution mechanism of fracture structure of loaded coal under different unloading rates,” *Meitan Xuebao/Journal China Coal Soc.*, vol. 45, pp. 3806–3816, 2020.
- [60] Y. Fu, X. Chen, and Z. Feng, “Characteristics of coal-rock fractures based on CT scanning and its influence on failure modes,” *Meitan Xuebao/Journal China Coal Soc.*, vol. 45, pp. 568–578, 2020.